Acta Cryst B
STRUCTURAL SCIENCE
CRYSTAL ENGINEERING
MATERIALS
ISSN 2052-5206

Neutron and high-pressure X-ray diffraction study of hydrogen-bonded ferroelectric rubidium hydrogen sulfate

HPSTAR 312-2016

Jack Binns,[a,b]*‡ Garry J McIntyre[a] and Simon Parsons[b]

[a]Australian Nuclear Science and Technology Organisation, New Illawarra Road, Lucas Heights, NSW 2234, Australia, and [b]EaStCHEM School of Chemistry and Centre for Science at Extreme Conditions, The University of Edinburgh, The King's Buildings, West Mains Road, Edinburgh EH9 3FJ, Scotland. *Correspondence e-mail: jack.binns@hpstar.ac.cn

Received 6 July 2016
Accepted 22 August 2016

Edited by F. P. A. Fabbiani, University of Göttingen, Germany

‡ Current affiliation: Center for High Pressure Science & Technology Advanced Research, Pudong, Shanghai, People's Republic of China

Keywords: ferroelectric; neutron diffraction; phase transitions.

CCDC references: 1500587; 1500588; 1500589; 1500590; 1500591; 1500592; 1500593

Supporting information: this article has supporting information at journals.iucr.org/b

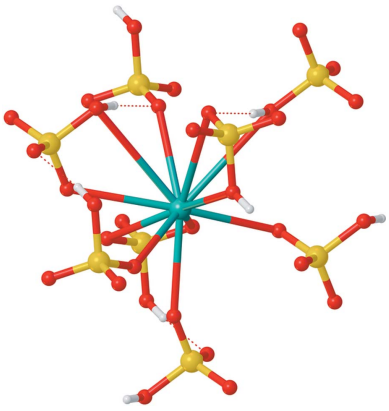

The pressure- and temperature-dependent phase transitions in the ferroelectric material rubidium hydrogen sulfate ($RbHSO_4$) are investigated by a combination of neutron Laue diffraction and high-pressure X-ray diffraction. The observation of disordered O-atom positions in the hydrogen sulfate anions is in agreement with previous spectroscopic measurements in the literature. Contrary to the mechanism observed in other hydrogen-bonded ferroelectric materials, H-atom positions are well defined and ordered in the paraelectric phase. Under applied pressure $RbHSO_4$ undergoes a ferroelectric transition before transforming to a third, high-pressure phase. The symmetry of this phase is revised to the centrosymmetric space group $P2_1/c$, resulting in the suppression of ferroelectricity at high pressure.

1. Introduction

Rubidium hydrogen sulfate ($RbHSO_4$) is one member of the family of solid-acid proton conductors, with the general formula $MHAO_4$, where $M = Na^+$, K^+, Rb^+, Cs^+ or NH_4^+ and A = S or Se. These materials have attracted attention as model hydrogen-bonded ferroelectric materials and for the superprotonic conduction phases achievable under relatively mild thermodynamic conditions.

Ferroelectric behaviour in $RbHSO_4$ was first reported by Pepinsky & Vedam (1960). Their efforts to understand ferroelectricity in ammonium hydrogen sulfate (NH_4HSO_4) focused on ordering within the N—H···O hydrogen bonds. To their surprise, isomorphous $RbHSO_4$ also showed a low-temperature ferroelectric phase without the requirement of cation–anion hydrogen bonds. Further measurements have shown ferroelectric transitions to be prevalent throughout the $MHAO_4$ family (Sinitsyn, 2010). Subsequent dielectric studies have revised the transition temperature, and recent piezo-response-force microscopy settled on the generally accepted Curie temperature of 264 K (Lilienblum *et al.*, 2013).

Initial structural investigations of $MHAO_4$ in general focused on low temperatures, and to some degree high pressures, in order to understand the ferroelectric transitions in these materials. Following the discovery of superprotonic conductivity, the high-temperature high-pressure regions of the PT phase diagrams were explored using electrical conductivity measurements (Ponyatovskii *et al.*, 1985). Collating over a range of M and A has allowed a general phase diagram to be produced (Sinitsyn, 2010). The phase diagram for $RbHSO_4$ is shown in Fig. 1.

Despite the topological similarity amongst the PT phase diagrams of members of the $MHAO_4$ family, corresponding

phases are not necessarily isostructural. $RbHSO_4$ and $RbHSeO_4$ share a phase sequence *superprotonic* → *paraelectric* → *ferroelectric*, which occurs at ambient pressure for $RbHSeO_4$ and at pressures ≥ 0.28 GPa in $RbHSO_4$, reflecting the 'chemical pressure' induced by substituting Se for S (Suzuki *et al.*, 1979). However, neither the paraelectric nor the ferroelectric phases are isostructural; $RbHSeO_4$ has space group $P1$ in the ferroelectric phase and $I2$ in the paraelectric phase (Waskowska *et al.*, 1980; Brach *et al.*, 1983), while the space groups of the corresponding phases in $RbHSO_4$ are Pc (phase II, ferroelectric) and $P2_1/c$ (phase I, paraelectric), respectively. In $RbHSeO_4$ the ferroelectric transition is due to proton ordering over a disordered hydrogen bond in contrast to the proposed mechanism, described below, in $RbHSO_4$ (Itoh & Moriyoshi, 2003).

The well studied analogue $CsHSO_4$ exhibits two ambient-pressure phases ($CsHSO_4$-II and $CsHSO_4$-III), both crystallize in $P2_1/c$, and therefore neither is ferroelectric. This material shows a very strong isotopic dependence with the metastable phase $CsHSO_4$-III only observed in the undeuterated form (Chisholm & Haile, 2000).

Pepinsky & Vedam (1960) performed the first structural characterization of $RbHSO_4$; they determined unit-cell parameters of phase I in both metrically pseudo-orthorhombic $B2_1/a$ and monoclinic $P2_1/c$ settings. They deduced that the ferroelectric transition from phase I to II requires the loss of the 2_1 screw symmetry element and determined that the ferroelectric phase must have symmetry Pc, later confirmed by systematic absence analysis (Pepinsky & Vedam, 1960).

The structures of phases I and II of $RbHSO_4$ were investigated using X-ray and neutron diffraction by Ashmore & Petch (1975). The neutron study revealed that the H-atom positions are fully ordered in the paraelectric phase, in contrast to paraelectric phases in analogous hydrogen-bonded ferroelectric materials. By analogy with the disorder–order transition observed in NH_4HSO_4, attempts were made to refine a disordered sulfate model, but the results were inconclusive.

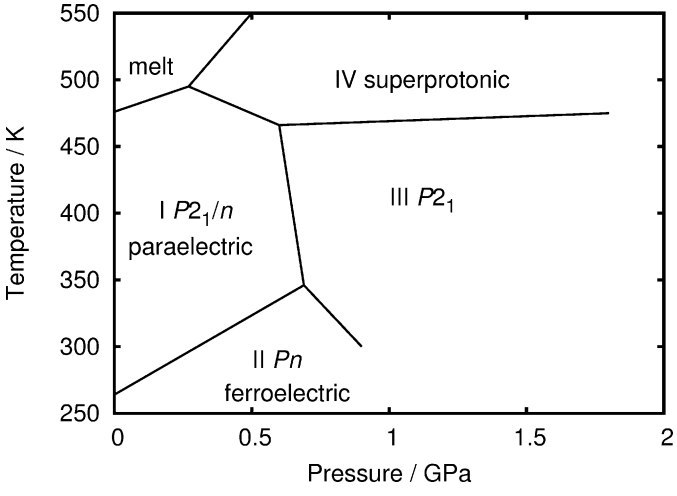

Figure 1
Pressure–temperature phase diagram of $RbHSO_4$ following Sinitsyn (2010, and references within). Phases I and II can also be described in $P2_1/c$ and Pc, respectively, by a different choice of unit-cell axes.

Dielectric measurements by Ozaki (1980) suggested that disorder should play an intrinsic role in the phase transition. In an attempt to confirm this, Itoh *et al.* (1995) report a disordered paraelectric structure for phase I, citing the large anisotropic displacement parameters of the O and H atoms of one HSO_4^- group, and the successful refinement of a disordered paraelectric phase of NH_4HSO_4, in support of the disordered model.

In a subsequent study, Itoh & Moriyoshi (2003) analysed the temperature dependence of thermal parameters above and below the Curie temperature, determining the ferroelectric structure for the first time. They conclude that one HSO_4^- anion shows disorder in two O-atom positions rather than all four. A Raman spectroscopy study by Toupry *et al.* (1981) found the temperature dependence of the O—H frequency to be consistent with a change in ionic orientation.

To complicate matters, an X-ray diffraction study by Nalini & Row (2003) has cast doubt on the disordered paraelectric model. They find no evidence of distortion in the sulfate geometries or significant residual electron density; they record notable distortions to the sulfate moieties only after cooling into the ferroelectric phase II.

While investigating the pressure dependence of the I → II transition, Gesi & Ozawa (1975) identified a high-pressure phase which was subsequently investigated by Asahi & Hasebe (1996) at pressures of 0.96 and 1 GPa; this phase III is described as monoclinic $P2_1$.

Clearly there remains some uncertainty as to the structure of the paraelectric phase I which modern neutron diffraction data can help to answer. State-of-the-art thermal–neutron Laue diffractometers allow the collection of extensive diffraction data to a similar precision as traditional monochromatic instruments with a gain in data collection rate of one-to-two orders of magnitude (McIntyre *et al.*, 2006). We show that this technique enables confirmation of the ordered proton positions as well as yielding accurate O—H bond lengths which help to clarify the mechanism of ferroelectricity in rubidium hydrogen sulfate.

2. Methods

Clear, block-like crystals of rubidium hydrogen sulfate ($RbHSO_4$) were grown from aqueous solutions of equimolar quantities of $RbSO_4$ and H_2SO_4.

X-ray diffraction data were collected on a Bruker SMART APEX II diffractometer with graphite-monochromated Mo $K\alpha$ radiation (λ = 0.71073 Å) equipped with an Oxford Cryosystems variable-temperature device. High-pressure X-ray diffraction experiments were carried out using a Merrill–Bassett diamond–anvil cell with a tungsten gasket and tungsten carbide backing plates with an accessible semi angle of 40° (Merrill & Bassett, 1974; Moggach *et al.*, 2008). The sample crystal and a chip of ruby were loaded with Fluorinert FC70 as the hydrostatic medium. The phase transition from I to II was initially found to occur on raising the pressure from 0 to

Table 1
Crystal data and details of the structure determination of $RbHSO_4$ phases I and II by neutron Laue diffraction.

For all structures: $HO_4S{\cdot}Rb$, M_r = 182.54, Z = 8. Experiments were carried out with neutron radiation, λ = 0.85–1.7 Å using the KOALA Laue diffractometer, ANSTO.

	Phase II	Phase I
Crystal data		
Crystal system, space group	Monoclinic, *Pn*	Monoclinic, $P2_1/n$
Temperature (K)	150	300
a, *b*, *c* (Å)†	14.2651 (5), 4.5853 (2), 14.2789 (5)	14.3602 (19), 4.6156 (6), 14.413 (2)
β (°)†	117.999 (2)	118.069 (8)
V (Å^3)†	824.66 (6)	842.9 (2)
Crystal size (mm)	1.20 × 1.10 × 0.80	1.20 × 1.10 × 0.80
Data collection		
No. of measured, independent and observed [$I > 2.0\sigma(I)$] reflections	13 194, 2365, 1909	8517, 1612, 1073
R_{int}	0.097	0.091
$(\sin\theta/\lambda)_{max}$ (Å^{-1})	1.114	1.113
Refinement		
$R[F^2 > 2\sigma(F^2)]$, $wR(F^2)$, S	0.048, 0.112, 0.96	0.051, 0.096, 0.91
No. of reflections	1909	1073
No. of parameters	253	146
No. of restraints	2	0
H-atom treatment	All H-atom parameters refined	All H-atom parameters refined
$\Delta\rho_{max}$, $\Delta\rho_{min}$ (fm Å^{-3})	0.64, −0.63	0.40, −0.41

Computer programs: MAATEL/ANSTO KOALA control program, *LaueG* (Piltz, 2016), *Laue*4 (Piltz, 2011), *argonne_boxes* (Wilkinson *et al.*, 1988), *SIR92* (Altomare *et al.*, 1993), *CRYSTALS* (Betteridge *et al.*, 2003). † Values derived from X-ray diffraction.

0.5 GPa. A second loading was used to fill in extra pressure points at 0.2 and 0.4 GPa, defining the transition pressure more precisely. Both loadings were carried out with crystals of similar sizes (0.10 × 0.12 × 0.20 and 0.10 × 0.15 × 0.20 mm). Pressure-dependent ruby fluorescence was used as a pressure measure (Piermarini *et al.*, 1975).

Diffraction data were integrated using *SAINT* (Bruker, 2007). Dynamic masks were applied to account for cell-body shading in the high-pressure data sets (Dawson *et al.*, 2004). Absorption corrections were carried out in *SADABS* (Sheldrick, 2008). The program *SHADE* was used to identify and discard partially shaded and diamond reflections (Parsons, 2004). Structures were solved by direct methods or charge flipping using *SIR*92 or *SUPERFLIP* (Altomare *et al.*, 1993; Palatinus & Chapuis, 2007).

Neutron Laue diffraction data were collected at 300 and 150 K at ambient pressure on the KOALA Laue diffractometer, at ANSTO, using a crystal of dimensions 1.2 × 1.1 × 0.8 mm. Laue patterns were collected for 4 h each; a total of 12 patterns were collected at 300 K, 14 at 150 K. In both cases the vertical rotation angle was 15° to account for the low symmetry of these crystals.

The diffraction patterns were indexed and processed using the program *LaueG* (Piltz, 2016). Reflection intensities were integrated with a modified two-dimensional version of the

Table 2
Bond distances and angles for $RbHSO_4$ phases I and II at 300 and 150 K, respectively.

Phase I (300 K)						
S1—O1	1.553 (5)	S1—O31	1.400 (14)	O1—H1	0.984 (4)	
S1—O30	1.481 (13)	S2—O8	1.453 (4)	S1—O21	1.505 (16)	
S2—O7	1.444 (5)	S1—O20	1.364 (18)	S2—O6	1.440 (4)	
S1—O4	1.439 (5)	S2—O5	1.567 (4)	O5—H2	0.990 (4)	
O1—S1—O4	108.4 (3)	O1—S1—O20	109.0 (9)	O1—S1—O30	96.9 (5)	
O1—S1—O21	105.4 (7)	O1—S1—O31	107.8 (7)	O4—S1—O20	117.2 (9)	
O4—S1—O30	108.4 (6)	O4—S1—O21	108.5 (7)	O4—S1—O31	116.2 (9)	
O5—S2—O8	104.0 (3)	O5—S2—O6	108.1 (2)	O5—S2—O7	105.5 (3)	
O7—S2—O8	112.7 (2)	O6—S2—O7	113.4 (3)	O6—S2—O8	112.3 (3)	
S1—O1—H1	111.7 (3)	S2—O5—H2	114.1 (2)			

Phase II (150 K)						
S1—O1	1.560 (6)	S1—O2	1.451 (6)	S1—O3	1.451 (6)	S1—O4	1.446 (7)
S2—O5	1.566 (6)	S2—O6	1.458 (6)	S2—O7	1.458 (6)	S2—O8	1.438 (8)
S3—O9	1.580 (7)	S3—O10	1.438 (7)	S3—O11	1.441 (6)	S3—O12	1.446 (8)
S4—O13	1.565 (5)	S4—O14	1.447 (6)	S4—O15	1.466 (6)	S4—O16	1.452 (7)
O1—H1	1.011 (6)	O5—H2	0.996 (6)	O9—H3	0.992 (6)	O13—H4	1.004 (6)
O1—S1—O2	105.9 (4)	O1—S1—O3	103.8 (4)	O1—S1—O4	108.5 (4)	O2—S1—O3	113.0 (4)
O2—S1—O4	112.6 (4)	O3—S1—O4	112.4 (4)	O5—S2—O8	106.7 (4)	O5—S2—O6	107.6 (3)
O5—S2—O7	103.9 (4)	O7—S2—O8	113.3 (4)	O6—S2—O7	111.5 (4)	O6—S2—O8	113.1 (4)
O9—S3—O11	102.6 (4)	O9—S3—O12	106.8 (4)	O9—S3—O10	107.1 (4)	O10—S3—O12	113.1 (5)
O11—S3—O12	112.8 (5)	O10—S3—O11	113.5 (5)	O13—S4—O14	108.2 (3)	O13—S4—O15	104.7 (4)
O13—S4—O16	105.4 (4)	O14—S4—O15	112.1 (4)	O14—S4—O16	113.4 (4)	O15—S4—O16	112.4 (3)
S1—O1—H1	113.5 (5)	S2—O5—H2	113.8 (4)	S3—O9—H3	108.4 (5)	S4—O13—H4	114.5 (4)

Table 3
Crystal data and details of the structure determination of $RbHSO_4$ phases I, II and III by high-pressure X-ray diffraction.

Phase	I	I	I	II	III
Pressure (GPa)	0.15 (10)	0.2 (1)	0.4 (1)	0.5 (1)	1.05 (10)
Crystal data					
Chemical formula	HO_4SRb	HO_4SRb	HO_4SRb	HO_4SRb	HO_4SRb
M_r	182.54	182.54	182.54	182.54	182.54
Crystal system, space group	Monoclinic, $P2_1/n$	Monoclinic, $P2_1/n$	Monoclinic, $P2_1/n$	Monoclinic, Pn	Monoclinic, $P2_1/c$
Temperature (K)	300	300	300	300	300
a, b, c (Å)	14.324 (3), 4.6263 (9), 14.401 (7)	14.3405 (7), 4.6150 (2), 14.3723 (12)	14.334 (5), 4.6197 (17), 14.361 (9)	14.166 (5), 4.5982 (9), 14.326 (4)	7.3202 (7), 7.765 (2), 7.3247 (8)
β (°)	117.74 (3)	118.054 (4)	118.94 (3)	117.68 (3)	110.938 (7)
V (Å^3)	844.6 (5)	839.42 (9)	832.2 (7)	826.4 (5)	388.85 (12)
Z	8	8	8	8	4
Radiation type	Mo $K\alpha$ (λ = 0.71073 Å)	Mo $K\alpha$ (λ = 0.71073 Å)	Mo $K\alpha$ (λ = 0.71073 Å)	Mo $K\alpha$ (λ = 0.71073 Å)	Mo $K\alpha$ (λ = 0.71073 Å)
μ (mm^{-1})	12.088	12.16	12.27	12.36	13.13
Crystal size (mm)	0.10 × 0.12 × 0.20	0.10 × 0.15 × 0.20	0.10 × 0.15 × 0.20	0.10 × 0.12 × 0.20	0.10 × 0.12 × 0.20
Data collection					
Diffractometer	Bruker Kappa APEX2	Bruker Kappa APEX2	Bruker Kappa APEX2	Bruker Kappa APEX2	Bruker Kappa APEX2
Absorption correction	Multi-scan *SADABS*	Multi-scan *SADABS*	Multi-scan *SADABS*	Multi-scan *SADABS*	Multi-scan *SADABS*
T_{min}, T_{max}	0.26, 0.30	0.09, 0.30	0.08, 0.29	0.24, 0.29	0.17, 0.27
No. of measured, independent and observed [$I > 2.0\sigma(I)$] reflections	3119, 754, 620	4260, 781, 673	4115, 754, 658	4613, 1240, 1149	1844, 295, 254
R_{int}	0.025	0.046	0.048	0.025	0.030
$(\sin\theta/\lambda)_{max}$ (Å^{-1})	0.617	0.595	0.588	0.620	0.602
Refinement					
$R[F^2 > 2\sigma(F^2)]$, $wR(F^2)$, S	0.023, 0.055, 1.02	0.056, 0.157, 0.99	0.069, 0.139, 1.04	0.044, 0.116, 0.83	0.032, 0.073, 0.98
No. of reflections	620	780	658	1149	254
No. of parameters	110	110	110	99	55
No. of restraints	0	20	28	2	13
H-atom treatment	H-atom parameters constrained	H-atom parameters constrained	H-atom parameters constrained	H-atom parameters constrained	H-atom parameters constrained
$\Delta\rho_{max}$, $\Delta\rho_{min}$ (e Å^{-3})	0.35, −0.35	1.03, −0.73	1.27, −0.99	0.84, −1.01	0.50, −0.35
Absolute structure	–	–	–	(Flack, 1983), 562 Friedel pairs	–
Absolute structure parameter	–	–	–	0.236 (18)	–

Computer programs: *APEX2* (Bruker, 2007), *SADABS* (Sheldrick, 2008), *SIR*92 (Altomare *et al.*, 1993), *CRYSTALS* (Betteridge *et al.*, 2003).

minimum $\sigma(I)/I'$ algorithm formulated by Wilkinson *et al.* (1988) and Prince *et al.* (1997). The data were normalized to a single common incident wavelength using the program *LAUE*4 for a wavelength spectrum of 0.85−1.7 Å (Piltz, 2011). For phase I, data were integrated to a resolution of d = 0.78 Å. A total of 8517 reflections were merged to a common incident wavelength giving an R_{merge} = 0.091 with a completeness of 77.1%. Data for phase II were integrated to a resolution of d = 0.67 Å. A total of 13 194 reflections were normalized and merged to a common incident wavelength with R_{merge} = 0.097 and a completeness of 74.3%. Laue diffraction suffers from intrinsic harmonic overlap that limits completeness values to a theoretical maximum of 83.3% (Cruickshank *et al.*, 1987, 1991). No absorption correction was applied due to the small crystal size and nearly spherical crystal form.

All structure refinements were carried out against $|F|^2$ in *CRYSTALS* (Betteridge *et al.*, 2003); initial atomic coordinates were derived from X-ray diffraction data. H atoms were refined with standard riding-model constraints in the refinements against X-ray data. In the refinements against neutron data, H-atom positional and anisotropic displacement parameters were refined freely. Unit-cell dimensions were taken from X-ray diffraction results at 150 and 300 K. Crystal and refinement data are given in Table 1. Selected bond lengths and angles for the different phases discussed in the following sections are compared in Table 2. Table 3 gives crystal and refinement details for refinements of high-pressure single-crystal X-ray diffraction data. Tables of the final refined atomic coordinates and displacement parameters are given in the supporting information.

3. Results and analysis

3.1. Ferroelectric phase II

The structure of rubidium hydrogen sulfate phase II was determined at 150 K in the non-standard polar space group Pn, with a = 14.2651 (5), b = 4.5853 (2), c = 14.2789 (5) Å, and β = 117.999 (2)°. In the standard Pc setting, used by Pepinsky

& Vedam (1960) and Itoh & Moriyoshi (2003), the unit-cell dimensions are a = 14.265, b = 4.585, c = 14.701 Å, and β = 120.955°. The *Pn* setting was used here on account of its (slightly) smaller value of β and because it makes the underlying pseudo-orthorhombic and pseudo-hexagonal symmetry more obvious through the near equality of a and c.

The final agreement factor for the refinement against the neutron diffraction data for phase II was low, $R[F^2 > 2\sigma(F^2)]$ = 0.048. Possibilities for twinning were investigated by coset decomposition, however, none of the applied twin laws improved data fitting.

Neutron diffraction data were refined against structures derived from ambient-pressure X-ray diffraction and the refined structures from each radiation are the same within error, with the exception of H-atom positions and displacement parameters. Geometric parameters quoted in the following discussion of the ambient-pressure structures are derived from neutron diffraction data.

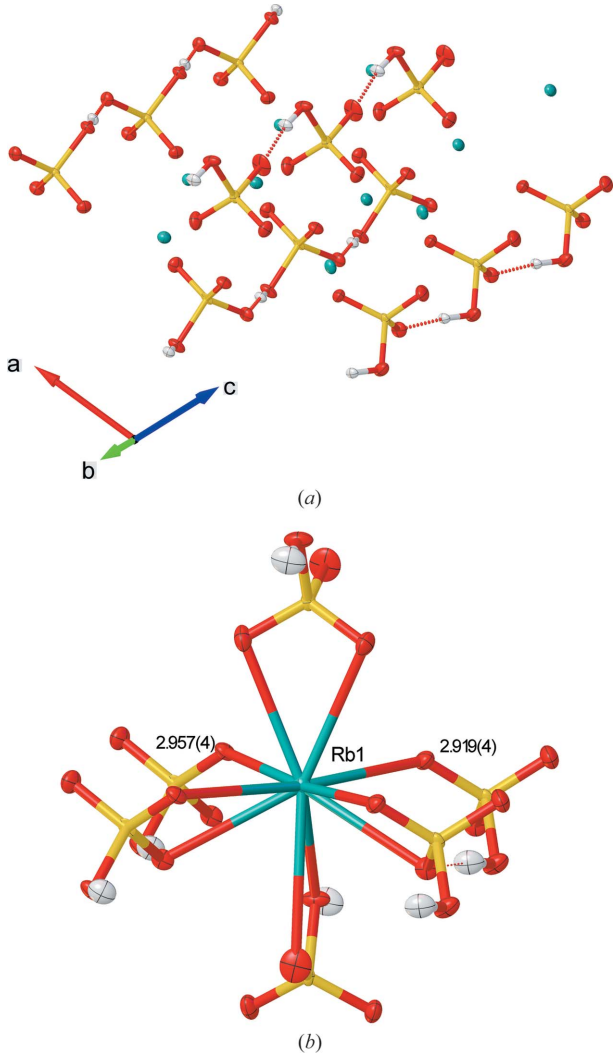

Figure 2
(*a*) Four unique hydrogen-bonded chains of hydrogen sulfate anions along the *b* axis in the asymmetric unit of phase II at 150 K; (*b*) the ten-atom coordination environment of Rb1, essentially identical to Rb2–4. The shortest Rb—O distances are given in the figure and are formed to the monodentate hydrogen sulfate anions. Rb: blue, S: yellow, O: red, H: white. Ellipsoids are shown at the 50% probability level.

The asymmetric unit in phase II consists of four rubidium cations and four hydrogen sulfate anions. HSO_4^- anions form infinite hydrogen-bonded chains in the *b* direction, running parallel to ribbons of Rb^+ cations (Fig. 2*a*). These chains have similar O···H distances of 1.551 (6) and 1.580 (7) Å, but different O—H···O angles of 174.2 (7) and 172.7 (6)° reflecting the two orientations adopted by the disordered anion on cooling. The S—O(—H) bond is elongated by 0.12 (1) Å on average relative to the other three S—O bonds and O—S—O bond angles range from 103.13 (12)° to 113.35 (15)°. The remaining 12 S—O bond lengths range in length from 1.438 (7) to 1.466 (6) Å. Each Rb^+ cation is coordinated by six HSO_4^- anions, four anions coordinate in a bidentate fashion, and the remaining two coordinate *via* a single O atom giving a total coordination number of ten (Fig. 2*b*). Rb—O coordination distances vary between 2.881 (4) and 3.443 (6) Å with the two shortest Rb—O bonds formed with the monodentate HSO_4^- anions. The origin of this structure was selected to match that of phase I to facilitate comparison.

3.2. Paraelectric phase I

At room temperature rubidium hydrogen sulfate has unit-cell dimensions a = 14.3602 (19), b = 4.6156 (6), c = 14.413 (2) Å, and β = 118.069 (8)°, space group $P2_1/n$, the non-standard setting chosen to give a smaller β angle closer to 90°.

The asymmetric unit of phase I contains two Rb^+ cations and two HSO_4^- anions. The hydrogen-bonded chains of anions observed in phase II persist in phase I, and indeed the structures of both phases are generally rather similar. Each HSO_4^- is distorted by the elongation of the S—O(—H) bond by 0.121 (4) Å. Beyond the elongation of the S—O(—H) bond, the remaining S—O bonds are statistically equal, bond angles within HSO_4^- units range from 103.60 (15)° to 116.7 (16)°. At 300 K, one rubidium cation (Rb1) is coordinated to six hydrogen sulfate anions in the same manner as at 150 K, four HSO_4^- bonding in a bidentate fashion, the remaining two being monodentate. The other Rb atom (Rb2) is nine-coordinate at 300 K, with three bidentate HSO_4^- and three monodentate HSO_4^- anions. Rb–O bond distances vary over a similar range to those in phase II, from 2.924 (3) to 3.256 (4) Å. The reduction in coordination number is caused by the shift in HSO_4^- orientation through the II–I transition, which results in a long Rb—O distance of 4.107 (4) Å compared with the bonding distance of 3.443 (6) Å in phase II. In phase I, both hydrogen-bonded chains are statistically similar, including the two hydrogen bonds formed by the disordered $HS(1)O_4^-$ anions. For $HS(1)O_4^-$ chains the O···H distance is 1.604 (14) Å to O30, and 1.521 (15) Å to O31, O—H···O angles are 170.3 (5) and 172.7 (5)°, respectively. Hydrogen-bonded chains formed by $HS(2)O_4^-$ anions have O···H distances of 1.610 (4) Å with an O—H···O angle of 171.2 (3)°.

In light of the disagreement in the literature regarding the disordered nature of the $HS(1)O_4^-$ anion, both ordered and

disordered models were refined against the neutron diffraction data for phase I, and the corresponding asymmetric units are shown in Figs. 3(*a*) and (*b*).

As Itoh & Moriyoshi (2003) note, anomalously large atomic displacement parameters (ADPs) are observed for the O atoms of the $HS(1)O_4^-$ tetrahedron, in particular O3 which acts as the donor in the O1—H1···O3 hydrogen-bonded infinite chain (Fig. 3*a*). This is clearly illustrated by comparison of the average equivalent isotropic displacement parameter (U_{eq}) for O atoms bound only to S [0.0456 (8) Å^2] and that of O3 [0.0707 (12) Å^2].

These results, along with earlier spectroscopic work by Ozaki (1980) and Toupry *et al.* (1981), are consistent with dynamic disorder in the two oxygen positions. Two O atoms of $HS(1)O_4^-$ can be refined against the neutron data obtained in the present study over two split positions each with refined occupancies of 0.51 (2) and 0.49 (2) for O20/21 and 0.50 (2) for O30/31. H atoms, located in difference maps, occupy well defined positions with no indication of split occupancy. The final agreement factor for the ordered model was R = 0.0552, that for the disordered model is R = 0.0508. This disordered model results in U_{eq} values for O30 and O31 that do not differ significantly from the average oxygen U_{eq} values, in contrast to the ordered model.

Below T_c, interaction between HSO_4^- ions outweighs thermal motion (Toupry *et al.*, 1981). The paraelectric to-ferroelectric transition therefore involves the ordering of two alternative anionic orientations representing minima between which $HS(1)O_4^-$ ions are able to oscillate in the paraelectric phase. Symmetry analysis using *ISODISTORT* (Campbell *et al.*, 2006) indicates that the phase I to II transition occurs *via* a ferroelectric mode of Γ_2^- symmetry, which is IR active, but Raman inactive. The absence of any mode softening as reported by Toupry *et al.* is in agreement with Raman and IR selection rules for this symmetry.

Comparison of the phase I and II structures in Figs. 3(*c*) and (*d*) shows the two disordered sites in the $HS(1)O_4$-I unit are overlapped orientations of the $HS(1)O_4$-II and $HS(3)O_4$-II units in the ferroelectric phase II. Fig. 3(*c*) shows two asymmetric units in phase I related by inversion symmetry. As the sample is cooled, half the $HS(1)O_4$-I units occupy the orientation of $HS(1)O_4$-II with the other half occupying the $HS(3)O_4$-II orientation as shown in Fig. 3(*d*). This breaks the inversion symmetry creating a non-centrosymmetric polar structure and giving rise to spontaneous electric polarization.

As is implied by the ferroic nature of this transition, this transition occurs *via* a *translationengeleiche* maximal group–subgroup relationship between phases I and II. In such a transition unit-cell dimensions remain essentially fixed and the point-group symmetry of the crystal is decreased (Müller, 2013).

3.3. High-pressure X-ray diffraction

$RbHSO_4$ is reported to undergo two phase transitions with pressure at room temperature. Above 0.4 GPa phase I ($P2_1/n$) undergoes a transition, which has been described as second-order (Kalevitch *et al.*, 1995; Itoh & Moriyoshi, 2003), to phase

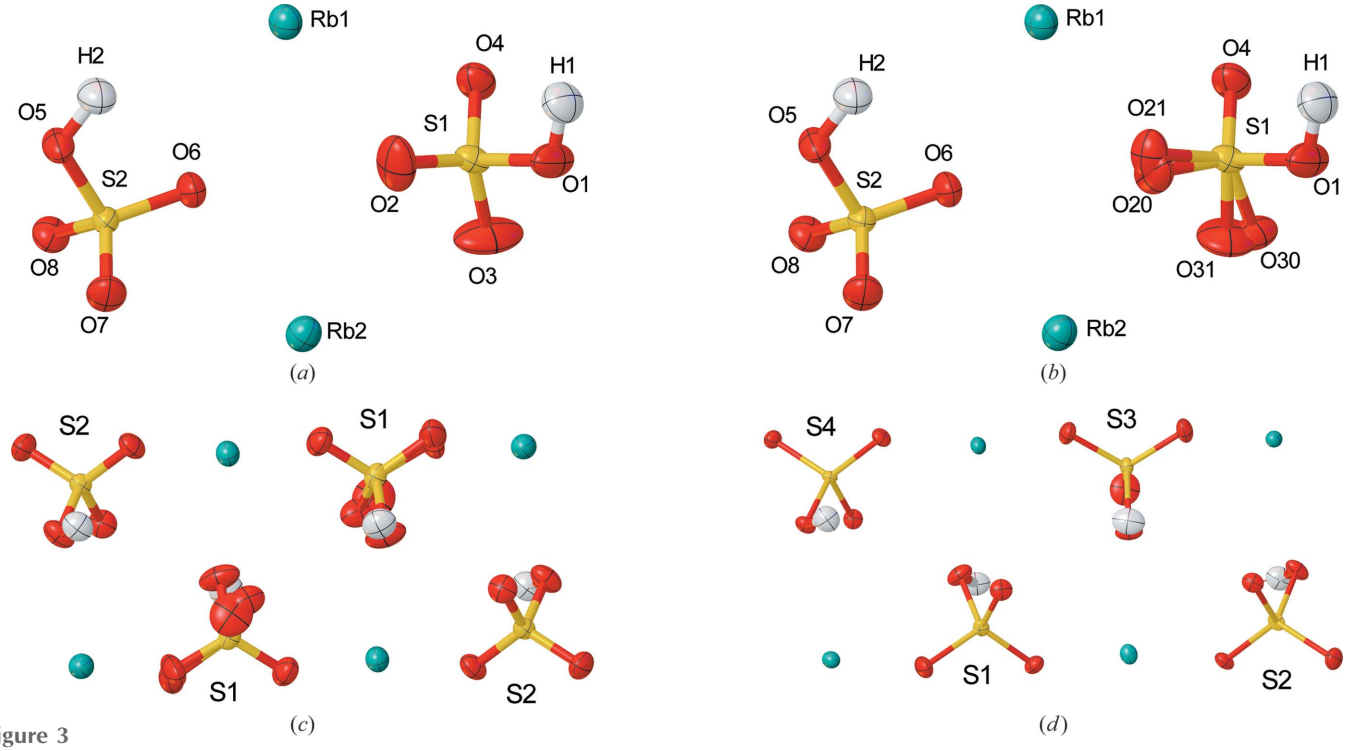

Figure 3
(*a*) Asymmetric unit of $RbHSO_4$ phase I, ordered model. The enlarged ADPs of O2 and O3 are clearly visible; (*b*) asymmetric unit of $RbHSO_4$ phase I, disordered model, splitting of O2 and O3 sites results in a lower R-factor and is supported by dielectric and solid-state NMR measurements. The two orientations of the disordered $HS(1)O_4$-I anions shown in (*c*) are approximately equivalent to the phase II anions $HS(1)O_4$-II and $HS(3)O_4$-II shown in (*d*).

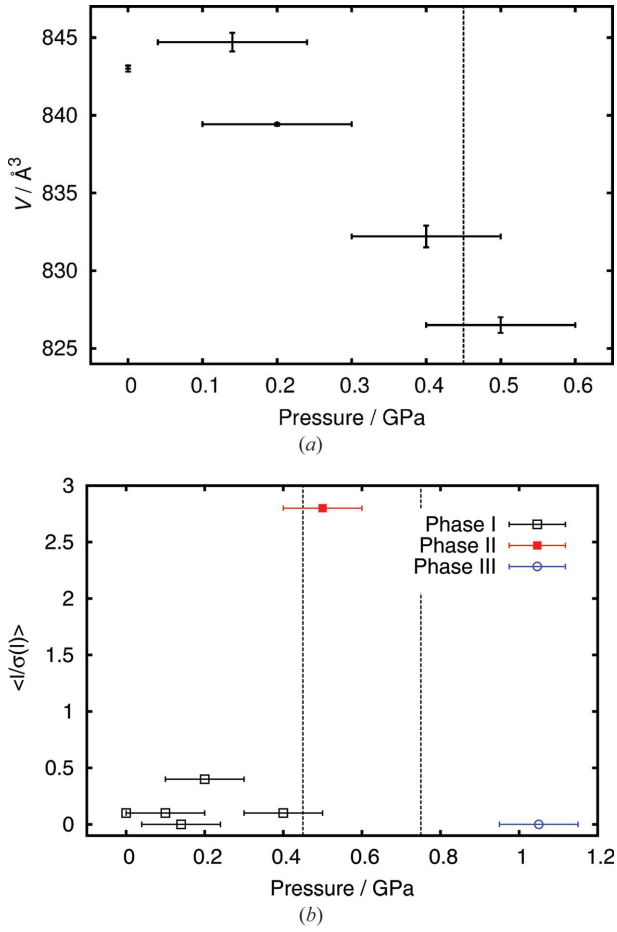

Figure 4
(*a*) Change in unit-cell volume for phases I and II with pressure; (*b*) change in $\langle I/\sigma(I)\rangle$ for reflections of the type $k = 2n + 1$, with pressure, showing the clear presence of a 2_1 screw symmetry element in phases I and III.

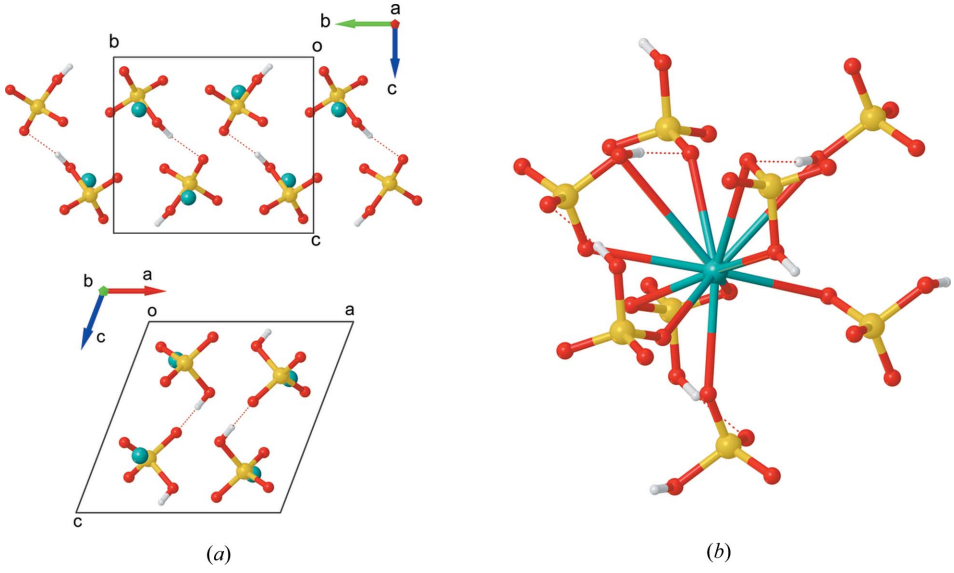

Figure 5
(*a*) Unit cell of $RbHSO_4$ phase III, two alternating HSO_4^- hydrogen-bonded chains form along the *c* axis; (*b*) coordination environment of Rb in phase III.

II (*Pn*), which then undergoes a first-order transformation at 0.75 GPa to phase III reported to be $P112_1$ (Asahi & Hasebe, 1996).

In this work single-crystal X-ray diffraction data were collected at pressures of 0.15 (10), 0.2 (1), 0.4 (1), 0.5 (1) and 1.05 (10) GPa.

Up to 0.4 GPa the unit-cell volume decreases by 10.8 (8) Å^3 (1.3%), axial compression is small, the most significant change is in *c* with a reduction of 0.052 (9) Å, *a* decreases by 0.026 (5) Å, and *b* remains unchanged within error. The β angle increases by 0.871 (3)° (0.73%). Over the I–II phase transition, the unit-cell volume falls continuously, β decreases by 1.26 (4)°, accompanied by decreases in *a* and *b* of −0.166 (7) and −0.021 (2) Å, respectively, and as a result the unit-cell volume falls by 5.7 (9) Å^3 (0.7%; Fig. 4*a*). Systematic absences were strongly suggestive of a loss of the 2_1 screw axis in phase II, although refinements were attempted in both $P2_1/n$ and *Pn*.

The structure of phase III has previously been described by Asahi & Hasebe (1996) as non-standard monoclinic, $P112_1$, a = 7.360 (4), b = 7.346 (4), c = 7.756 (2) Å, γ = 110.86 (4)° at 1.00 (3) GPa. The present X-ray diffraction measurements at 1.1 (1) GPa have found phase III to be monoclinic, $P2_1/c$, a = 7.3202 (7), b = 7.765 (2), c = 7.3247 (8) Å, β = 110.938 (7)°.

The change in $\langle I/\sigma(I)\rangle$ for reflections of the type $k = 2n + 1$ with pressure is shown in Fig. 4(*b*), indicating the presence of the 2_1 screw symmetry element in phases I and III. For phase II, refinement in $P2_1/n$ resulted in a significantly higher agreement factor, R = 0.0991 *versus* R = 0.0437 in *Pn*, confirming the systematic absence analysis. The resulting structure for phase III is similar to that described by Asahi & Hasebe (1996), although with space-group symmetry reassigned (Fig. 5). Of the 279 reflections affected by the presence of *c*-glide symmetry, three have $I/\sigma(I) > 3$, $\langle I/\sigma(I)\rangle = 0.5$, $\langle I\rangle$ = 0.3. This structure is isostructural with the corrected structure of $CsHSO_4$-II reported by Chisholm & Haile (2000).

The diffraction pattern showed clear signs of pseudo-merohedral twinning, with two domains indexed to the above cell related by a twofold rotation about the [$\bar{1}$01] direction, and reflections are related by the twin law expressed below, as determined using the program *CELL NOW* (Sheldrick, 2005).

$$\begin{pmatrix} 0 & 0 & \bar{1} \\ 0 & \bar{1} & 0 \\ \bar{1} & 0 & 0 \end{pmatrix}$$

The twinning reflects the pseudo-orthorhombic symmetry of the lattice (present because $a \simeq c$) leading to a two-domain twin. The refined twin scale factor was

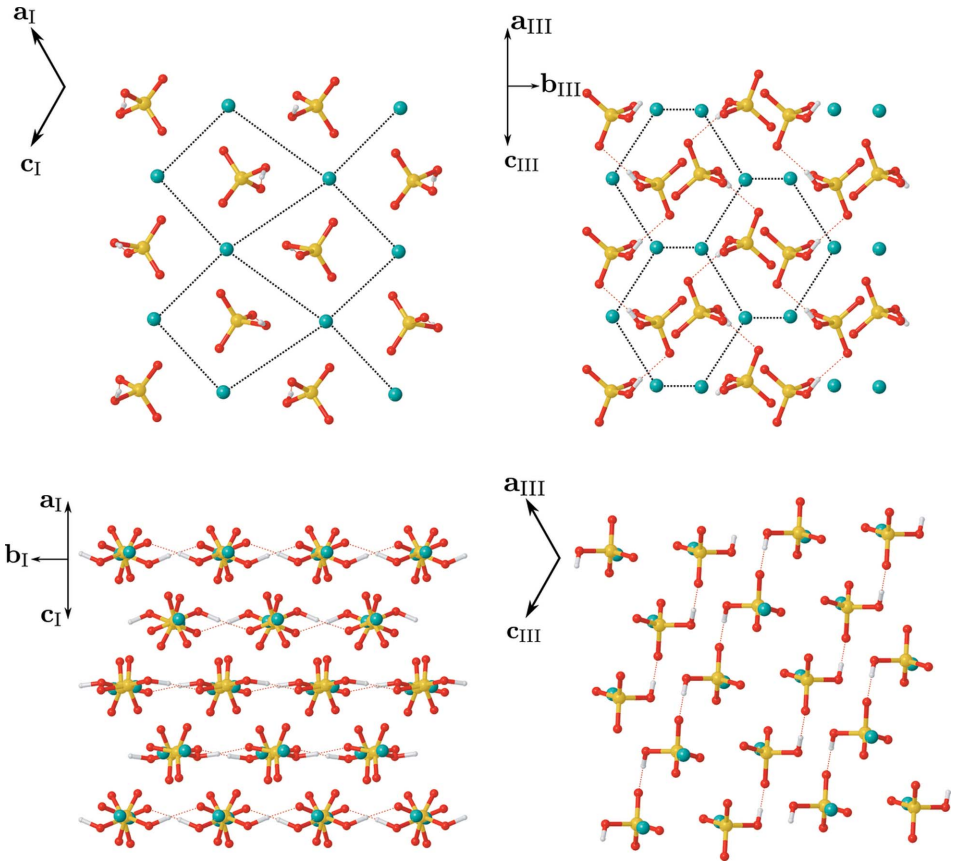

Figure 6
Reorientation of Rb^+ cations and HSO_4^- anions through the pressure-induced phase transition. (*a*) Illustrates the asymmetric diamond channels in phase I, shifts in Rb^+ positions leading to the formation of staggered hexagonal channels containing reoriented HSO_4^- anions. (*b*) Formation of a new hydrogen-bonding system in phase III. The linear chains along $\mathbf{b}_I$ are broken by the movement of HSO_4^- anions to form new zigzagging chains along the $\mathbf{c}_{III}$ direction.

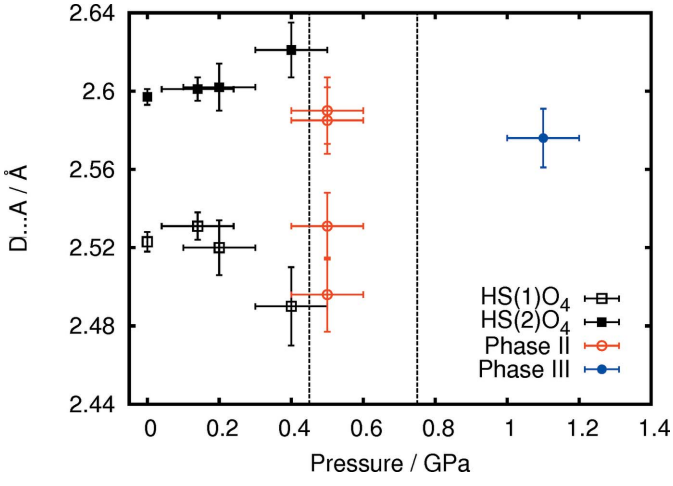

Figure 7
Changes in hydrogen bonding donor–acceptor distances ($D\cdots A$) with pressure in $RbHSO_4$. The two symmetry-independent hydrogen-bonded chains in phase I are shown by open and closed black squares. Phase II data are shown by open red circles. Phase III datum is shown by a closed blue circle.

0.541 (11). Given the very minor structural differences between phases I and II, the following discussion of the structural changes is applicable to both I and II.

The rows of cations along the $[101]_{III}$ direction (equivalent to $[010]_I$) are preserved through the transition, with a shift in Rb^+ positions occurring within the ac_I plane (equivalent to the [101]-$\mathbf{b}_{III}$ plane). The Rb^+ cations shift by $\pm$ 0.99 (2) Å along the $[101]_I$ direction (along $\mathbf{b}_{III}$) in an alternating fashion, forming corrugated hexagonal nets parallel to $(100)_{III}$. As a result, the asymmetric diamond-shaped channels in the $\mathbf{b}_I$ direction (along which the infinite $HSO_4^-\cdots HSO_4^-$ chains form) transform to staggered hexagonal channels to accommodate the HSO_4^- reorientations shown in Fig. 6. Accompanying this shift, the HSO_4^- anions reorient, breaking the infinite hydrogen-bonded chains along $\mathbf{b}_I$. The new arrangement consists of two symmetry-related, zigzagging infinite chains along the $\mathbf{c}_{III}$ direction, with an O(H)$\cdots$O distance of 2.576 (15) Å. These new chains form at an angle of $\beta_{III}/2 = 55.5^\circ$ to the direction of the chains in phase I. As a result, the asymmetric diamond-shaped channels in the $\mathbf{b}_I$ direction (along which the infinite $HSO_4^-\cdots HSO_4^-$ chains form) transform to staggered hexagonal channels to accommodate the HSO_4^- reorientations. The alternating chain direction regenerates the inversion symmetry of phase I, removing the polarization present in phase II.

There are no statistically significant changes to bond lengths within the HSO_4^- anions up to 1.1 GPa. In phase III, rubidium cations are coordinated by 11 O atoms, an increase in coordination number of one as shown in Fig. 5(*b*). Two HSO_4^- anions bind in a bidentate fashion through two O atoms, the remaining anions bind in a monodentate manner. Rubidium–oxygen bonds adopt a wider range of lengths in this phase, from 2.861 (9) to 3.589 (12) Å, and as a result the average Rb—O bond length [3.121 (9) Å] is the same within error as at ambient pressure [3.077 (3) Å]. This is an example of the widely observed 'pressure–distance paradox' whereby pressure-driven coordination number increases are accompanied by an increase in bond length (Kleber & Wilke, 1969).

The pressure response of donor–acceptor distances are shown in Fig. 7. Up to 0.4 GPa the hydrogen-bonding distances in the $HS(1)O_{4,I}$ and $HS(2)O_{4,II}$ chains remain

distinct with the difference in O(H)···O distances increasing from 0.074 (6) Å at ambient pressure to 0.13 (2) Å at 0.4 GPa. Upon the transition to phase II, O(H)···O distances are not statistically distinguishable for each symmetry-independent chain. The increase in symmetry over the phase II → III transition means that phase III contains only one unique hydrogen bond, in which the O(H)···O distance is 2.576 (15) Å, which is not significantly different to the ambient-pressure values. Table 3 lists selected crystal structure determination details for each phase at high pressure.

4. Conclusions

The paraelectric → ferroelectric transition in $RbHSO_4$ has been investigated with neutron Laue diffraction. H atoms were refined to singly occupied positions with no sign of possible double-well occupancy. One HSO_4^- moiety could be refined with two disordered O atoms; this disordered model resulted in better agreement with the neutron data over an ordered model with distended oxygen ADPs. Pressure-driven phase transitions were investigated by a single-crystal X-ray diffraction isothermal pressure series up to 1.1 (1) GPa. The first-order reconstructive phase transition from ferroelectric phase II to phase III was investigated, and the space group revised from $P2_1$ and $P2_1/c$.

Acknowledgements

We thank the Bragg Institute, ANSTO, for the allocation of neutron beamtime under proposal 3588. JB wishes to thank EPSRC and the Australian Government for funding.

References

Altomare, A., Cascarano, G., Giacovazzo, C. & Guagliardi, A. (1993). *J. Appl. Cryst.* **26**, 343–350.
Asahi, T. & Hasebe, K. (1996). *J. Phys. Soc. Jpn*, **65**, 3233–3236.
Ashmore, J. & Petch, H. (1975). *Can. J. Phys.* **53**, 2694–2702.
Betteridge, P. W., Carruthers, J. R., Cooper, R. I., Prout, K. & Watkin, D. J. (2003). *J. Appl. Cryst.* **36**, 1487.
Brach, I., Jones, D. J. & Rozière, J. (1983). *J. Solid State Chem.* **48**, 401–406.
Bruker (2007). *APEX*2. Bruker AXS Inc., Madison, Wisconsin, USA.
Campbell, B. J., Stokes, H. T., Tanner, D. E. & Hatch, D. M. (2006). *J. Appl. Cryst.* **39**, 607–614.
Chisholm, C. R. & Haile, S. M. (2000). *Mater. Res. Bull.* **35**, 999–1005.
Cruickshank, D. W. J., Helliwell, J. R. & Moffat, K. (1987). *Acta Cryst.* A**43**, 656–674.
Cruickshank, D. W. J., Helliwell, J. R. & Moffat, K. (1991). *Acta Cryst.* A**47**, 352–373.
Dawson, A., Allan, D. R., Parsons, S. & Ruf, M. (2004). *J. Appl. Cryst.* **37**, 410–416.
Flack, H. D. (1983). *Acta Cryst.* A**39**, 876–881.
Gesi, K. & Ozawa, K. (1975). *J. Phys. Soc. Jpn*, **38**, 459–462.
Itoh, K. & Moriyoshi, C. (2003). *Ferroelectrics*, **285**, 91–104.
Itoh, K., Ohno, H. & Kuragaki, S. (1995). *J. Phys. Soc. Jpn*, **64**, 479–484.
Kalevitch, N. I., Arnscheidt, B., Pelzl, J. & Rodin, S. V. (1995). *J. Mol. Struct.* **348**, 361–364.
Kleber, W. & Wilke, K. T. (1969). *Kristallogr. Techn.* **4**, 165–199.
Lilienblum, M., Hoffmann, Á., Soergel, E., Becker, P., Bohatý, L. & Fiebig, M. (2013). *Rev. Sci. Instrum.* **84**, 043703.
McIntyre, G. J., Lemée-Cailleau, M.-H. & Wilkinson, C. (2006). *Physica B*, **385–386**, 1055–1058.
Merrill, L. & Bassett, W. A. (1974). *Rev. Sci. Instrum.* **45**, 290–294.
Moggach, S. A., Allan, D. R., Parsons, S. & Warren, J. E. (2008). *J. Appl. Cryst.* **41**, 249–251.
Müller, U. (2013). *Symmetry Relationships between Crystal Structures: Applications of Crystallographic Group Theory in Crystal Chemistry.* Oxford University Press.
Nalini, G. & Row, T. N. G. (2003). *Phase Transitions*, **76**, 923–934.
Ozaki, T. (1980). *J. Phys. Soc. Jpn*, **49**, 234–241.
Palatinus, L. & Chapuis, G. (2007). *J. Appl. Cryst.* **40**, 786–790.
Parsons, S. (2004). *SHADE.* The University of Edinburgh, Scotland.
Pepinsky, R. & Vedam, K. (1960). *Phys. Rev.* **117**, 1502–1503.
Piermarini, G. J., Block, S., Barnett, J. & Forman, R. (1975). *J. Appl. Phys.* **46**, 2774–2780.
Piltz, R. (2011). *Acta Cryst.* A**67**, C155.
Piltz, R. O. (2016). Personal communication.
Ponyatovskii, E. G., Rashchupkin, V. I., Sinitsyn, V. V., Baranov, A. I., Schuvalov, L. A. & Shchagina, N. M. (1985). *JETP Lett.* **41**, 139–141.
Prince, E., Wilkinson, C. & McIntyre, G. J. (1997). *J. Appl. Cryst.* **30**, 133–137.
Sheldrick, G. M. (2005). *CELL NOW.* University of Göttingen, Germany, and Bruker AXS Inc, Madison, Wisconsin, USA.
Sheldrick, G. M. (2008). *SADABS* 2008/1. University of Göttingen, Germany.
Sinitsyn, V. V. (2010). *J. Mater. Chem.* **20**, 6226–6234.
Suzuki, S., Osaka, T. & Makita, Y. (1979). *J. Phys. Soc. Jpn*, **47**, 1741–1742.
Toupry, N., Poulet, H. & Le Postollec, M. (1981). *J. Raman Spectrosc.* **11**, 81–91.
Waskowska, A., Olejnik, S., Lukaszewicz, K. & Czapla, Z. (1980). *Cryst. Struct. Commun.* **9**, 663–669.
Wilkinson, C., Khamis, H. W., Stansfield, R. F. D. & McIntyre, G. J. (1988). *J. Appl. Cryst.* **21**, 471–478.